

See discussions, stats, and author profiles for this publication at: <https://www.researchgate.net/publication/234381694>

# Photodissociation Dynamics of $C_2H_2$ , $C_2D_2$ , and $C_2HD$ at 121.6 nm

ARTICLE in THE JOURNAL OF PHYSICAL CHEMISTRY A · SEPTEMBER 1997

Impact Factor: 2.69 · DOI: 10.1021/jp970536f

---

CITATIONS

12

---

READS

7

3 AUTHORS, INCLUDING:



Jeng-Han Wang

National Taiwan Normal University

46 PUBLICATIONS 999 CITATIONS

SEE PROFILE

# Photodissociation Dynamics of C<sub>2</sub>H<sub>2</sub>, C<sub>2</sub>D<sub>2</sub>, and C<sub>2</sub>HD at 121.6 nm

Jeng-Han Wang

Department of Chemistry, National Taiwan University, Taipei, Taiwan 10764

Yen-Tsung Hsu, and Kopin Liu\*

Institute of Atomic and Molecular Sciences, Academia Sinica, Taipei, Taiwan 10764

Received: February 11, 1997; In Final Form: April 14, 1997<sup>®</sup>

The product translational energy distribution  $P(E_t)$  and the recoil anisotropy parameter  $\beta(E_t)$  for acetylene (and isotopic variants) photodissociation at 121.6 nm have been obtained by detecting the H(D) atom fragment using the Doppler-selected time-of-flight (TOF) technique. A strong propensity toward the formation of the C<sub>2</sub>H( $\tilde{A}^2\Pi$ ) fragment was revealed. The resolution of this technique is sufficiently high to resolve the vibrational structures of a small polyatomic molecule. The vibrational spectroscopic constants of the C–H and C–C stretching modes for the C<sub>2</sub>H( $\tilde{A}^2\Pi$ ) state were obtained for the first time, and the mode-specific vibrational state distributions were deduced. It is conjectured that two distinct dissociation pathways, arising from the Rydberg–valence surface intersections, are involved in the title processes. The branching of these two pathways is governed by the initial absorption step.

## I. Introduction

Acetylene (C<sub>2</sub>H<sub>2</sub>) is one of the simplest hydrocarbons with chemistry highly relevant to a number of natural or man-made phenomena occurring in interstellar processes and combustion, and as such its spectroscopy and photochemistry in the UV and VUV regions have received considerable attention. The 190–250-nm absorption region is assigned to a weak, linear to trans-bent transition ( $\tilde{A}^1A_u \leftarrow \tilde{X}^1\Sigma_g^+$ ).<sup>1,2</sup> The spectrum is dominated by a long progression of the in-plane bending and C≡C stretching modes. Fluorescence from the  $\tilde{A}$ -state has also been observed.<sup>3,4</sup> A sudden falloff of the fluorescence quantum yield occurs around 214.3–215.8 nm, which was initially attributed to the predissociation of C<sub>2</sub>H<sub>2</sub> to C<sub>2</sub>H + H. A value of  $132.97 \pm 0.48$  kcal/mol was then inferred for  $D_0(\text{H}–\text{C}_2\text{H})$ , which is just slightly larger than the most accurate value of  $131.73 \pm 0.02$  kcal/mol obtained more recently by the Rydberg H-atom TOF measurement.<sup>5</sup> A recent reinvestigation<sup>6</sup> combining the fluorescence quantum yield and photofragment yield measurements confirms the earlier fluorescence quenching data, which, however, casts some doubts on the original interpretation. Instead, the involvement of the triplet manifold in the  $\tilde{A}$ -state predissociation is suggested.

In the VUV region the 165–195-nm spectrum is assigned to the  $\tilde{B}^1B_u \leftarrow \tilde{X}^1\Sigma_g^+$  transition,<sup>7</sup> spectra become richer at even shorter wavelengths and several (ro)vibrationally resolved Rydberg series and valence states have been identified.<sup>8–10</sup> Because both C<sub>2</sub>H<sub>2</sub> and C<sub>2</sub>H<sub>2</sub><sup>+</sup> are linear in the ground states and only the C–C bond length changes significantly from 1.20 Å (C<sub>2</sub>H<sub>2</sub>) to 1.26 Å (C<sub>2</sub>H<sub>2</sub><sup>+</sup>), all Rydberg transitions of C<sub>2</sub>H<sub>2</sub> exhibit a strong  $\nu_2$  progression (totally symmetric C≡C stretching mode). Near the hydrogen Lyman- $\alpha$  (L- $\alpha$ ) transition at 121.6 nm the vibronic Rydberg state denoted as  $3R''(^1\Pi_u)2_0^1$  is most relevant.<sup>9</sup> This band is diffuse because of predissociation. With 10.2-eV photon energy three fragmentation channels, the formation of C<sub>2</sub> + H<sub>2</sub>, 2CH, and C<sub>2</sub>H + H, are energetically accessible. This work focuses on the characterization of H-atom elimination. Because the excitation of C<sub>2</sub>H<sub>2</sub> at 121.6 nm involves a vibronically resolved Rydberg state, the study of its

dissociation dynamics offers an opportunity to elucidate the Rydberg–valence interactions<sup>11–15</sup> and to explore the photochemical consequence of Rydbergization<sup>15</sup> in a complementary manner to the spectroscopic means which are sensitive only to the Franck–Condon region.

Although the photochemical behaviors of C<sub>2</sub>H<sub>2</sub> in the VUV region are more poorly characterized than in the UV region, it is anticipated that the majority, if not all, of those excited states, eventually lead to dissociation with the ethynyl radical (C<sub>2</sub>H) being one of the major primary products. The understanding of the photodissociation of C<sub>2</sub>H<sub>2</sub> and the subsequent reactions of C<sub>2</sub>H are of central importance in photochemical models of planetary atmospheres<sup>16,17</sup> and in hydrocarbon combustion chemistry.<sup>18</sup> For example, in combustion of fossil fuels the ethynyl radical is involved in the formation of polyacetylenes and possibly of polycyclic aromatic hydrocarbons (PAHs) and hence of soot. The reaction of C<sub>2</sub>H with NO may also be of importance to NO<sub>x</sub> chemistry.<sup>19</sup> In modeling interstellar clouds and planetary atmospheres, such as Titan's, the reaction of C<sub>2</sub>H with acetylene to form diacetylene (C<sub>4</sub>H<sub>2</sub>),<sup>20–22</sup> which is a key precursor to the formation of polyacetylene hazes and ices,<sup>23</sup> is of particular importance. The reaction of C<sub>2</sub>H with CH<sub>4</sub> has also been suggested to catalyze the decomposition of CH<sub>4</sub>.<sup>24</sup> The recombination of two methyl radicals then produces ethane, which is an abundant species in Titan's atmosphere. Further reactions of C<sub>2</sub>H<sub>6</sub> with C<sub>2</sub>H and CH<sub>3</sub> can lead to the formation of C<sub>3</sub>H<sub>8</sub>; similarly for the formation of a host of larger hydrocarbons. In addition, the participation of C<sub>2</sub>H in the networks of organic chemistry of interstellar medium could also have relevance for events leading the origin of life on Earth.<sup>16</sup> Hence, the photochemistry of C<sub>2</sub>H<sub>2</sub>, among a few others such as CH<sub>4</sub>, plays a decisive role in our fundamental understanding of present interstellar atmospheres and possibly their past evolution.

In all these chemical models the reaction rate coefficients used to date assume that C<sub>2</sub>H is in the electronic ground state,  $\tilde{X}^2\Sigma^+$ . However, in a recent communication<sup>25</sup> we reported that the photodissociation of C<sub>2</sub>H<sub>2</sub> at 121.6 nm yielded predominantly the low-lying, electronically excited C<sub>2</sub>H( $\tilde{A}^2\Pi$ ). This remarkable propensity against the formation of electronic ground

<sup>®</sup> Abstract published in *Advance ACS Abstracts*, July 1, 1997.

state of  $\text{C}_2\text{H}$  at L- $\alpha$  has also been found by Wittig and co-workers using the Rydberg H-atom TOF technique.<sup>26</sup> In addition, they also reported the same propensity for the excited  $\tilde{\text{A}}$ -state of  $\text{C}_2\text{H}_2$  using an elegant IR–UV excitation scheme.<sup>26</sup> It appears that the preferential formation of the  $\text{C}_2\text{H}(\tilde{\text{A}})$  fragment may be quite common when  $\text{C}_2\text{H}_2$  is irradiated by a VUV photon. The reactivities of  $\text{C}_2\text{H}$  in the  $\tilde{\text{A}}$   $^2\Pi$  state are unknown at the present time but can be quite different from those in the ground state. Since chemical models of interstellar clouds and combustion processes are based on the knowledge of the rates and products of important reactions, the astrochemical and combustion implications of this finding await further investigations and model analysis.

Reported here is the full account of our previous communication.<sup>25</sup> The details of our experimental approach, Doppler-selected TOF (a 3-D mapping) technique, will be given. The improved results for  $\text{C}_2\text{H}_2$  will be presented. In combination with those extended for  $\text{C}_2\text{D}_2$  and  $\text{C}_2\text{HD}$  isotopic variants, a clearer picture about the photodissociation mechanisms emerges.

## II. Experimental Section

**(A) Methodology.** A complete characterization of the dynamics of photodissociation or collisional processes involves the determination of the state-to-state differential cross section. Toward this goal an approximately “single state” of  $\text{C}_2\text{H}_2$  reagent is prepared by supersonic expansion means in this study, and the product state-resolved differential cross section is achieved by a 3-D mapping method for characterizing the product H-atom c.m. (center of mass) 3-D velocity distribution with resolution sufficiently high so that the internal state distribution of the polyatomic cofragment  $\text{C}_2\text{H}$  can be revealed as structures in the H-atom measurement. The 3-D mapping method, Doppler-selected time-of-flight (TOF) technique,<sup>25</sup> is essentially a “core-sampling” approach by combining three independent 1-D projection methods in an orthogonal manner: the Doppler shift (frequency dispersion) for  $v_z$  selection, the ion time-of-flight (temporal dispersion) for  $v_y$  measurement, and the slit (spatial dispersion) for  $v_x$  restriction, as depicted in Figure 1. In brief, at a certain probe laser wavelength ions generated via a REMPI detection process represent a 2-D product velocity distribution in an  $X$ – $Y$  plane with a constant  $v_z$  component selected by the Doppler-shift technique. Ions within this 2-D slice are conventionally collected as one data point in a Doppler profile, as indicated with a square mark in Figure 1. Rather than collecting all those ions, a slit is placed in front of the ion detector (where the plane of space-focusing lies) to restrict detection of ions with  $v_x \approx 0$ , which leaves only a 1-D distribution of  $v_y$  to be dispersed and measured by using an ion TOF method. A complete recovery of the 2-D distribution can readily be achieved by a rotation operation of the measured  $v_y$  distribution around  $\hat{z}$  provided that the cylindrical symmetry is preserved along the  $Z$  axis, as demonstrated in a recent crossed-beam scattering experiment.<sup>27</sup> In case such a symmetry is absent, as in some configurations for photodissociative studies, the loss of  $v_x$  information can still be recovered by a proper combination of TOF spectra obtained with different photolysis laser polarizations (i.e.,  $\perp$  and  $\parallel$  with respect to the TOF axis), *vide infra*. Scanning the probe laser wavelength allows successive 2-D distributions to be obtained for the subsequently  $v_z$ -selected slices. The recombination of these 2-D slices will then directly reproduce the desired complete 3-D velocity distribution.

**(B) Apparatus.** The experiments were conducted in a pulsed, crossed-beam apparatus detailed previously.<sup>28</sup> For the present work, only a single beam was employed. The isotopic samples,

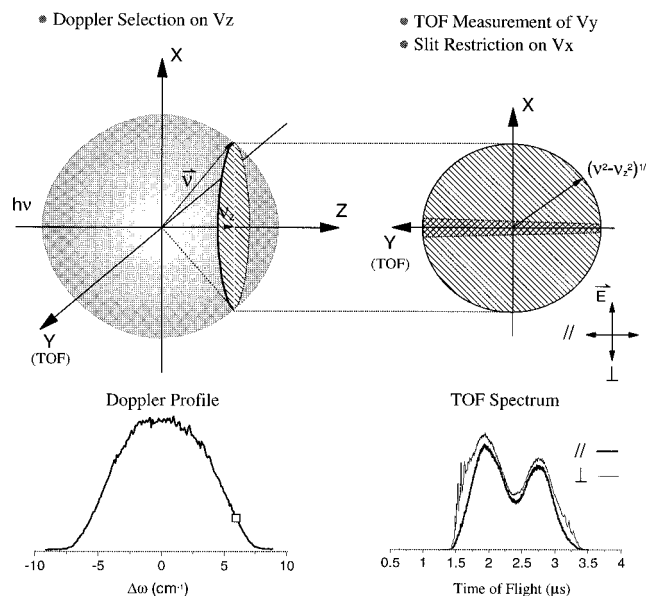


**Figure 1.** Schematics illustrating the basic concept of the Doppler-selected TOF technique. The hatched slice represents a Doppler-selected 2-D velocity distribution for a certain  $v_z$ . The gray strip on the 2-D slice is the 1-D distribution measured by TOF technique under the restriction of a slit. The corresponding collective and TOF-dispersed signals are illustrated in the lower parts by a square mark on the Doppler profile and two TOF spectra, respectively.

$\text{C}_2\text{HD}$  and  $\text{C}_2\text{D}_2$  (Cambridge Isotope Lab, 90% isotopic purity and 98% chemical purity for  $\text{C}_2\text{HD}$ , and 99% D for  $\text{C}_2\text{D}_2$ ), were used directly from the gas cylinder, whereas  $\text{C}_2\text{H}_2$  was used either with or without a freeze-and-thaw procedure for the removal of the acetone impurity. In the latter cases no differences in the resulting TOF spectra could be detected. To minimize the chemical interferences for clustering, which could readily be observed as VUV photoionized cluster peaks when the spectrometer was operated in the mass mode, mild expansion (neat and  $\leq 1$  atm backing pressure) was used in all cases. To minimize the difference between the c.m. and laboratory velocity frames, the beam was directed nearly collinear ( $18^\circ$ ) with respect to the laser propagation axis.

The detection of H/D photofragments was achieved by using (1+1) REMPI via L- $\alpha$  transition at 121.6 nm. The 121.6-nm photon, which also served as the photolysis light source (i.e., a one-color experiment), was produced by the third harmonic generation scheme in a Kr gas cell<sup>29</sup> and then recollimated by a LiF lens—rather than the LiF window used in the previous report.<sup>25</sup> This lens implementation significantly improved the TOF resolution by reducing the higher order effects from the initial spatial-spread of the ion packet. The change of polarization of the VUV photo was accomplished by inserting a  $\lambda/2$  waveplate after a Glan laser polarizer in the UV beam path. The so-called “parallel” and “perpendicular” polarizations are referenced to the ion TOF axis. A single-stage TOF arrangement was devised for measuring the ion speed distribution. Figure 2 depicts the current TOF device, which differs from the old version reported previously<sup>25</sup> in dimensions. It consists of a repeller, an extractor, and a field-free region (D) and is a rather simple and compact device. The temporally dispersed ions were then detected by a chevron MCP, signal amplified and recorded on a 500-MHz transient digital oscilloscope (LeCroy 9350). The overall temporal resolution of our apparatus, including lasers and electronics, was measured to be about 3 ns.

A few comments are worthwhile mentioning about the present setup. First, the approach of our ion TOF measurement is to

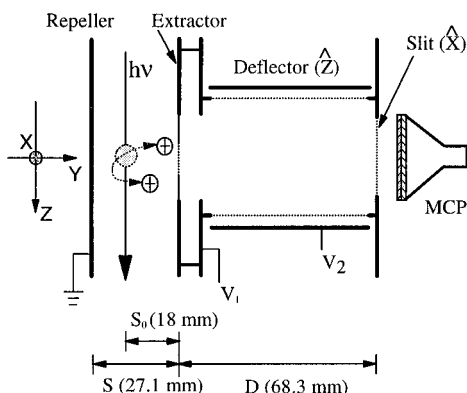


Figure 2. Schematic of the single-stage TOF device.

use a large ionization volume for reducing the space charge effects and then to take advantage of the space-focusing technique to compress the spatially spread ion packet for recovering the temporal, thus translational energy, resolution. The dimensions of the single-stage TOF device were set up by the first-order space-focusing condition:  $2U_0 + 2S_0E_s = E_sD$ , where  $U_0$  is the initial kinetic energy to be measured,  $S_0$  the distance between the ionization center and the extractor,  $E_s$  the ion draw-out field, and  $D$  the ion free drift distance. The actual dimensions used in the time-to-speed transformation were determined from the calibration experiments. Thus, contrary to the widely accepted Wiley–McLaren two-stage setup,<sup>30</sup> the space-focusing condition here is largely fulfilled over a range of  $U_0$  by the geometrical factors. By simply varying the extraction voltage the best compromise between the resolution and S/N ratio can readily be achieved, as illustrated in Figure 3a for a portion of the spectra under different extraction voltages. Second, although an unfocused laser was used, to our surprise the power density was still intense enough to make the space charge effects discernible, as shown in Figure 3b, presumably due to the large absorption cross sections. Systematic examination of the space charge effects reveals that the resolution gets worse first, followed by a broadening of the overall TOF profile. Third, in addition to the mentioned 3-D velocity mapping scheme, the more familiar 2-D<sup>31</sup> and 1-D<sup>32,33</sup> spectra can also be obtained. By using a boxcar to integrate the ion signals while scanning the probe laser, the resulting, low-field Doppler spectrum corresponds to the central-strip distribution obtained from the 2-D image technique. On the other hand, operation of the TOF device under a high extraction field, say 700 V/cm in the present case, will permit detection of all ions without  $v_x/v_y$  discrimination. Then, it acts as a usual TOF mass spectrometer and the conventional Doppler (1-D projection) profile will then be measured. Hence, the present single-stage TOF arrangement is intrinsically simple and flexible, which allows 1-D, 2-D, and 3-D measurements to be performed all in a single setup.

**(C) Data Analysis.** The c.m. differential cross section for a single-photon, dissociative process can be expressed as<sup>34,35</sup>

$$f(\vec{v}) = \frac{d^3\sigma}{dv d\Omega} = \frac{1}{4\pi} g(v) [1 + \beta(v) P_2(\cos \theta)] \quad (1)$$

where  $\theta$  is the angle between the fragment recoil velocity and the polarization axis of dissociating light and  $P_2(\cos \theta) = (3 \cos^2 \theta - 1)/2$ . The goal is then to determine  $g(v)$  and  $\beta(v)$  experimentally. Three experimental configurations are particularly informative using the Doppler-selected TOF technique. If the probe laser wavelength is chosen such that only those ions

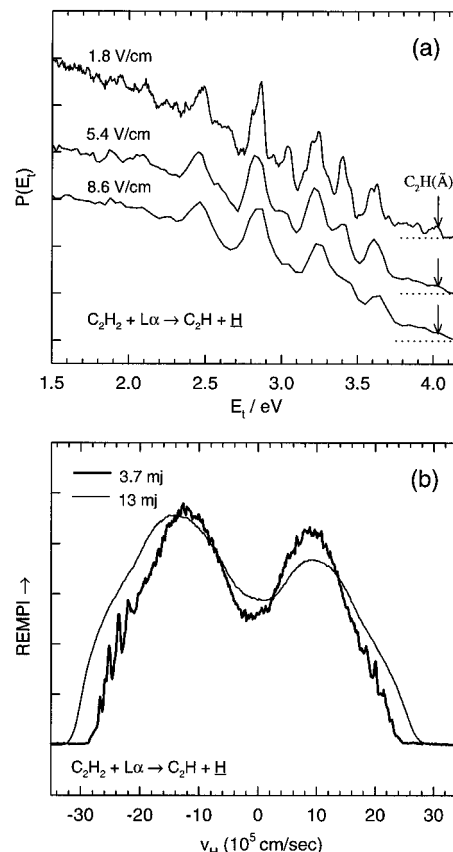


Figure 3. (a)  $P(E_i)$  distributions for the photolysis of C<sub>2</sub>H<sub>2</sub>, obtained with differing extraction field strengths. The best energy resolution achieved at the extraction field of  $\sim 1.8$  V/cm is in accord with the first-order space focusing equation. (b) TOF-dispersed velocity distributions illustrating space charge effects. The higher UV laser power (13 mJ) results in a broadened profile and loss of the structural features.

with  $v_z = 0 \pm \Delta v_z$  ( $\Delta v_z$  determined by the laser bandwidth) will be ionized in the REMPI process and the slit restricts further only those ions with  $v_x \approx 0 \pm \Delta v_x$  ( $\Delta v_x$  determined by the slit width and the ion arrival time) to be detected, then one has a nominally 1-D speed distribution  $f(v_y; v_z \approx 0, v_x \approx 0)$ . Recasting eq 1 in Cartesian coordinates and omitting the  $1/4\pi$  factor, it becomes for  $\theta = 0^\circ$ , i.e., ||-polarization,

$$f^{\parallel}(v_y; v_x \approx v_z \approx 0) = g(v) [1 + \beta(v)] \quad (2)$$

for  $\theta = 90^\circ$ , i.e.,  $\perp$ -polarization,

$$f^{\perp}(v_y; v_x \approx v_z \approx 0) = g(v) [1 - \frac{1}{2}\beta(v)] \quad (3)$$

and for  $\theta = 54.7^\circ$ , i.e., magic-angle,

$$f^m(v_y; v_x \approx v_z \approx 0) = g(v) \quad (4)$$

Hence, one has

$$g(v) = f^m = (f^{\parallel} + 2f^{\perp})/3 \quad (5)$$

$$\beta(v) = 2(f^{\parallel} - f^{\perp})/(f^{\parallel} + 2f^{\perp}) \quad (6)$$

And the product translational energy distribution becomes

$$P(E_i) = d\sigma/dE_i \propto g(v)/v \quad (7)$$

where  $E_t$  is the product translational energy and is related to the translational energy ( $E$ ) of the fragment being detected by  $E_t = E(M/(M - m))$  with  $m$  being the detected fragment mass and  $M$  the molecular precursor mass.

The remaining task is to relate the desired  $f(v_y)$  to the corresponding TOF profile  $D^i(T)$ , where the origin of the flight time ( $T_0$ ) is set at  $v_y = 0$ . It should be noted that both Doppler-shift ( $v_z$ ) and ion TOF ( $v_y$ ) act directly in the c.m. velocity frame, and the small  $v_x$ -component of the parent molecule speed ( $2.7 \times 10^4$  cm/s) makes the difference between the c.m. and laboratory frames negligibly small. Furthermore, what is measured in this experiment corresponds to the density of the distribution in the c.m. velocity space,  $D(v_x, v_y, v_z)$ . Since the density is invariant with respect to the coordinate systems used in the velocity space, i.e.,  $d\vec{v} = dv_x dv_y dv_z = v^2 dv d\Omega$ , in terms of the differential cross section one has  $D(v_x, v_y, v_z) = d^3\sigma/dv_x dv_y dv_z = d^3\sigma/v^2 dv d\Omega = f(\vec{v})/v^2$ . Under the core sampling conditions, i.e.,  $v_x \approx v_z \approx 0$ , the measured TOF profile is then given approximately by

$$D^i(T)\Delta T = \int \frac{f(\vec{v})}{v^2} d\vec{v} \approx f(v_y; v_x \approx v_z \approx 0) \Delta v_x \Delta v_y \Delta v_z / v^2 \quad (8)$$

or

$$f(v_y; v_x \approx v_z \approx 0) \approx D^i(T) \frac{\Delta T}{\Delta v_y} \cdot \frac{v^2}{\Delta v_x \Delta v_z} \quad (9)$$

where  $\Delta v_z$  arises from the finite laser bandwidth in Doppler selection,  $\Delta v_z = \omega_0 \Delta \omega / c$ ,<sup>32</sup> which is a constant;  $\Delta v_x$  comes from the finite slit width ( $\Delta h$ ) which can be accounted for on the 1-D "solid angle" consideration as  $\Delta v_x = 1/2 \Delta h / t$  with  $t$  being the ion arrival time. The term  $\Delta T / \Delta v_y$  is the time-to-speed transformation, which is usually a linear function under the space-focusing conditions.<sup>30,33</sup> However, a significant deviation from linearity is observed when the ion extraction voltage approaches or is less than the initial energy release, as in the present case. The exact transformation according to the overall flight time of ions is then used in the data analysis.

What is outlined above is an inversion procedure to obtain  $g(v)$  (or  $P(E_t)$ ) and  $\beta(v)$  directly from the Doppler-selected TOF spectra. However, L- $\alpha$  is a doublet optical transition. Its complication needs to be dealt with before one can proceed to the inversion analysis. The L- $\alpha$  doublet splitting of  $0.365 \text{ cm}^{-1}$  corresponds to  $\Delta v_z = 1.34 \times 10^5 \text{ cm/s}$  in speed. In other words the situation corresponds to having two identical Newton spheres separated from each other by  $\Delta v_z$ . At a given wavelength, Doppler selection actually samples two subgroups of H-fragments with Doppler shifts differing by  $\Delta v_z$ . As illustrated in Figure 4a, subgroups *a* and *b* are Doppler-selected at  $\omega_C$ , so are subgroup *b* and *c* at  $\omega_B$  and subgroup *c* and *d* at  $\omega_A$ . Recall that subgroup *b* contributes to both the Doppler-selected TOF spectra obtained at  $\omega_B$  ( $^2P_{3/2} \leftarrow ^2S_{1/2}$  transition) and  $\omega_C$  ( $^2P_{1/2} \leftarrow ^2S_{1/2}$  transition) with an intensity ratio of 2 to 1. The subtraction of the TOF spectrum obtained at  $\omega_C$  by one-half of that obtained at  $\omega_B$  will consequently cancel the contribution from subgroup *b*. The resultant TOF spectrum contains a major contribution from subgroup *a* and a remaining negative contribution from subgroup *c*. The contamination from subgroup *c* can then be eliminated by successive addition of one-quarter of the TOF spectrum obtained at  $\omega_A$ . The subtraction/addition procedure can be so forth repeated until the remaining higher terms become negligible. The general form of this scheme can

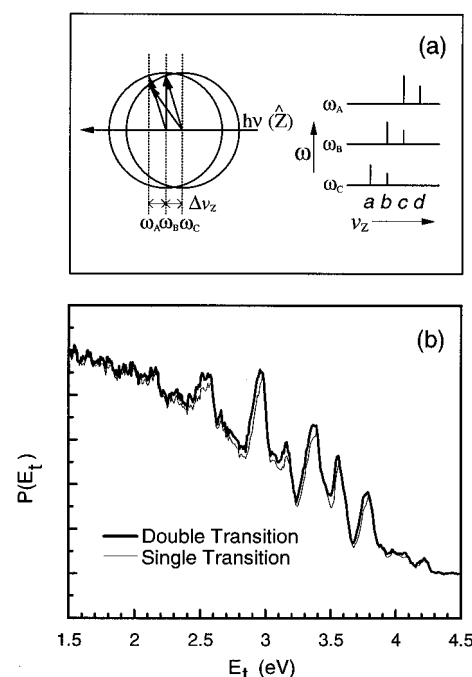


**Figure 4.** (a) Two corresponding Newton spheres separate on the laser axis by  $\Delta v_z$  (i.e.,  $1.34 \times 10^5 \text{ cm/s}$ ) due to the doublet nature of L- $\alpha$  transition. Notations *a, b, c,* and *d* represent the velocity subgroups in the elucidation of the subtraction/addition scheme for eliminating the doublet complication. See text for detail. (b)  $P(E_t)$  distributions for the photolysis of  $\text{C}_2\text{H}_2$  before and after the subtraction/addition scheme was applied. After the removal of the doublet complication the resultant single transition spectrum displays slightly improved energy resolution.

be expressed as

$$\text{TOF}_\omega^S = \text{TOF}_\omega^D - \frac{1}{2} \text{TOF}_{\omega+\Delta\omega}^D + \frac{1}{4} \text{TOF}_{\omega+2\Delta\omega}^D - \frac{1}{8} \text{TOF}_{\omega+3\Delta\omega}^D + \dots \quad (10)$$

where the superscript S denotes the single optical transition, the superscript D the doublet transitions, and  $\Delta\omega$  the frequency difference between doublet transitions ( $0.365 \text{ cm}^{-1}$ ).

Alternatively, owing to the symmetry properties of photo-dissociation from a one-photon dipole transition, a simpler scheme can be obtained,

$$\text{TOF}_{\omega_0}^S = 2\text{TOF}_{\omega_0}^D - \text{TOF}_{\omega_0-\Delta\omega}^D \quad (11)$$

where  $\omega_0$  denotes the frequency corresponding to the center of the Newton sphere for the  $^2P_{3/2} \leftarrow ^2S_{1/2}$  optical transition. The necessity of this complication is demonstrated in Figure 4b, if one seeks to achieve the high-resolution results.

The inversion procedure outlined above implicitly assumes the validity of both space-focusing and core-sampling conditions. The former requirement is largely met by the geometric factors of the single-stage TOF spectrometer, while the latter needs some practical considerations. The maximum speed of the H-fragment in the photodissociation of  $\text{C}_2\text{H}_2$  at L- $\alpha$  is  $2.89 \times 10^6 \text{ cm/s}$ , which will yield a Doppler width of  $15.8 \text{ cm}^{-1}$ . The probe laser bandwidth (FWHM) is about  $0.3 \text{ cm}^{-1}$  in VUV, which corresponds to a Doppler-selected  $\Delta v_z$  of  $5.5 \times 10^4 \text{ cm/s}$ . The slit width of the current setup is 3 mm and the ion arrival time ranges from 2.4 to  $4.0 \mu\text{s}$  (Figure 6a);  $\Delta v_x$  is thus no more than  $6.3 \times 10^4 \text{ cm/s}$ . Accounting for the effects of both  $\Delta v_x$  and  $\Delta v_z$ , therefore, the core-sampling conditions should hold for  $v > 8.4 \times 10^4 \text{ cm/s}$  or  $E_t > 4 \text{ meV}$ . Considering the simplicity of the inversion procedure (no simulation!) and the negligibly small range over which the core-sampling breaks

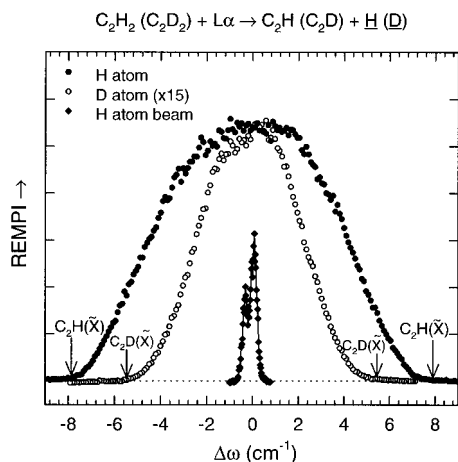


**Figure 5.** Doppler profiles of H and D fragments from the photolysis of C<sub>2</sub>H<sub>2</sub> and C<sub>2</sub>D<sub>2</sub>, respectively. The narrow doublet at the center is the Doppler profile of a supersonically cooled H-atom beam.

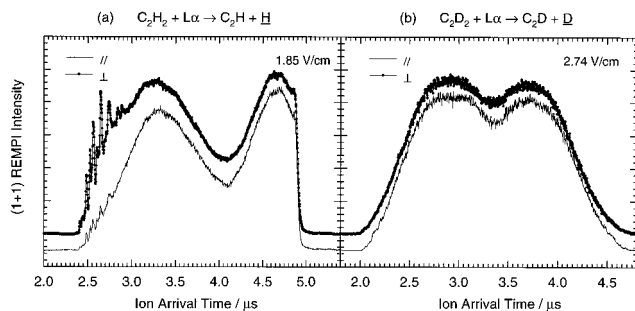


**Figure 6.** Raw TOF spectra for the photolysis of (a) C<sub>2</sub>H<sub>2</sub> and (b) C<sub>2</sub>D<sub>2</sub>, obtained with two polarization configurations. The laser frequency was set at the center of the Doppler profile, i.e.,  $\omega_0$ .

down, all the results to be presented adapt the data analysis described above.

### III. Results and Discussion

**(A) C<sub>2</sub>H<sub>2</sub> and C<sub>2</sub>D<sub>2</sub>.** The (1-D projection) Doppler profiles of H and D fragments from the photolysis of C<sub>2</sub>H<sub>2</sub> and C<sub>2</sub>D<sub>2</sub>, respectively, are shown in Figure 5. As readily seen both fragments' profiles are broad and structureless. The difference in widths, however, cannot be entirely accounted for by the simple mass ratio, which suggests significantly different fragment 3-D velocity distributions of the two processes. Arrows marked in Figure 5 indicate energetic limits associated with the electronic ground state of C<sub>2</sub>H/C<sub>2</sub>D cofragments, which appear to be slightly larger than the maximal Doppler shift of the corresponding profile.

The two profiles were obtained back-to-back and under otherwise identical conditions, which allowed the relative yields of H and D fragments to be estimated,  $H(C_2H_2)/D(C_2D_2) \approx 25$ . Using the photofragment action spectroscopic technique, Welge and co-workers<sup>36</sup> recently showed that the absorption of C<sub>2</sub>H<sub>2</sub> at the H-atom L- $\alpha$  line is in exact resonance with the  $(3R'' \leftarrow \tilde{X})2_0^1$  transition, whereas that of C<sub>2</sub>D<sub>2</sub> at the D-atom L- $\alpha$  line lies in the broad, weak continuum spectral region. Thus, the observed large disparity in photofragment yield of the H- vs D-atom can be attributed to the difference in the initial photoexcitation step of two isotopic molecules.

Figure 6a displays raw TOF spectra of H-atom fragments for two different polarization configurations. The spectra were obtained with an ion extraction field of 1.85 V/cm at *ca.*  $\omega_0$ , i.e., nominally  $v_z \approx 0$ . The two spectra were normalized to each other by using high field measurements as mentioned in

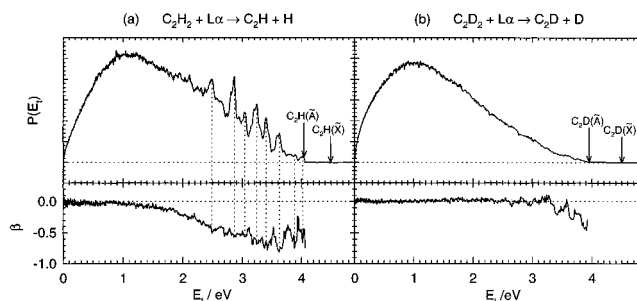


**Figure 7.** Photofragment c.m. translational energy distribution  $P(E_t)$  and anisotropy distribution  $\beta(E_t)$  for the photolysis of (a) C<sub>2</sub>H<sub>2</sub> and (b) C<sub>2</sub>D<sub>2</sub>. The arrows mark the energetic thresholds for the corresponding electronic states of the fragment C<sub>2</sub>H/C<sub>2</sub>D. The out-of-phase correlation between the mild oscillations of  $\beta$  and the structures in  $P(E_t)$  is indicated by vertical dashed lines.

the Experimental Section. Clearly, the  $\perp$  configuration yields slightly higher intensity than the  $\parallel$ , and structures are seen in both configurations for the fast-moving fragments with the  $\perp$  configuration far more prominent. The dips in the TOF spectra (at about 4.1  $\mu$ s ion arrival time, referred to as  $T_0$ ) correspond to the ions with initial kinetic energy  $U_0 = 0$ . Ions coming to the detector later than  $T_0$  are those with an initial velocity in the opposite direction to the detector, so-called return ions. The clip-off on return ions at  $\sim 4.9 \mu$ s was due to collision with the repeller plate before turnaround occurred. Similar spectra for C<sub>2</sub>D<sub>2</sub> are shown in Figure 6b, which differ substantially from those of C<sub>2</sub>H<sub>2</sub> in that they exhibit no clear structures and display nearly identical shapes for the two polarizations. The complete collection of return ions for C<sub>2</sub>D<sub>2</sub> was due to the use of an old version of the TOF setup which had different dimensions from the current one. The experiment for C<sub>2</sub>H<sub>2</sub> performed under the identical condition as that shown in Figure 6b yielded a spectrum with a resolution slightly better than that for 5.4 V/cm shown in Figure 3a, thus, the lack of structures for the C<sub>2</sub>D<sub>2</sub> case is not due to the different experimental setups.

The data analysis follows the inversion procedures described earlier. The final results for the product translational energy distribution  $P(E_t)$  and recoil anisotropy  $\beta(E_t)$  for the C<sub>2</sub>H<sub>2</sub> and C<sub>2</sub>D<sub>2</sub> cases are shown in Figure 7. Clearly, the two cases differ significantly in both aspects. Contrary to the case of C<sub>2</sub>H<sub>2</sub>, the product translational energy distribution for C<sub>2</sub>D<sub>2</sub> is structureless, which indicates very different dissociation mechanisms from C<sub>2</sub>H<sub>2</sub>. In spite of that, both distributions show a clear propensity against the formation of C<sub>2</sub>H( $\tilde{X}$ ) from photodissociation. The behaviors of the recoil anisotropy parameters  $\beta(E_t)$  also differ. The angular distribution for the C<sub>2</sub>D<sub>2</sub> case is isotropic except near the onset of the formation of the C<sub>2</sub>D( $\tilde{A}$ ) state, whereas the  $\beta$ -values for the C<sub>2</sub>H<sub>2</sub> case exhibit a distinct dependence on product translational energy, ranging from zero for slowly moving products to about  $-0.8$  near the observed, energetic threshold. The negative  $\beta$  value is consistent with the previous spectroscopic assignment of a perpendicular transition for the initial excitation of C<sub>2</sub>H<sub>2</sub> ( $\tilde{X}^1\Sigma_g^+ \rightarrow R''(^1\Pi_u)$ ),<sup>8</sup> and its magnitude suggests a rather prompt dissociation process. As argued previously, at least two possibilities can result in such an energy dependence of  $\beta$  values. It can be attributed to a range of dissociation times compared to the parent molecular rotation time scale, resulting in a more effective energy randomization and more rotational depolarization of the fragment spatial distribution.<sup>34,37</sup> However, considering the light mass of the H-fragment this possibility seems unlikely for a supersonic cooled parent molecule. Alternatively, there are in fact two distinct dissociation pathways with different  $\beta$  parameters and the energy dependence of the observed  $\beta$  values arises

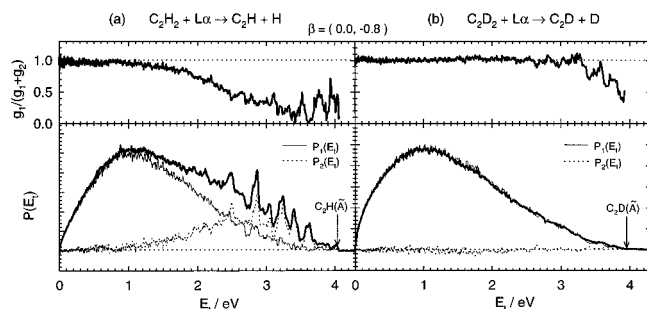


**Figure 8.** Partitioned  $P(E_i)$  for the photolysis of (a)  $C_2H_2$  and (b)  $C_2D_2$  under the assumption of  $\beta_1 = 0$  and  $\beta_2 = -0.8$ . The upper panels show the resulting branching fraction, while the lower panels display the fragment translational energy distributions of the two corresponding pathways.

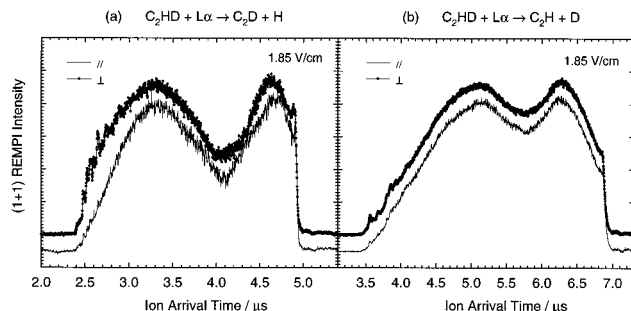


**Figure 9.** Raw TOF spectra for the photolysis of  $C_2HD$  when the (a) H- or (b) D-fragment was detected with two polarization configurations. The laser frequency was set at the center of the Doppler profile, i.e.,  $\omega_0$ .

from the energy dependence of the branching ratio of these two pathways. As presented previously the observed correlation between the structures in  $\beta$  value and those in  $P(E_i)$  distribution reinforces this scenario.

Accordingly, eqs 5 and 6 can be shown to be

$$g(\nu) = g_1(\nu) + g_2(\nu) \quad (12)$$

$$\beta(\nu) = \chi(\nu) \beta_1 + (1 - \chi(\nu)) \beta_2 \quad (13)$$

respectively, where  $\chi(\nu) = g_1(\nu)/(g_1(\nu) + g_2(\nu))$  denotes the branching fraction of two dissociation pathways. With the assumption of  $\beta_1 = 0$  and  $\beta_2 = -0.8$ , the results of two dissociation pathways, i.e.,  $g_1$ ,  $g_2$ , and  $\chi$ , are shown in Figure 8. These two pathways are distinguished from each other by the different dissociation time scales with respect to the internal motions of the photoexcited parent molecules. Not surprisingly, the dissociation of  $C_2D_2$  is almost entirely via the slow pathway. On the other hand, for  $C_2H_2$  the prompt dissociation yields the fast fragments with a highly structured translational energy distribution and the slow dissociation pathway produces slower fragments with a structureless distribution as for  $C_2D_2$ . In fact, the two  $P(E_i)$ 's of the slow components for  $C_2H_2$  and  $C_2D_2$  are nearly superimposable. Integrating  $P_1(E_i)$  and  $P_2(E_i)$  for  $C_2H_2$  yields the branching ratio of these two pathways, i.e., a ratio of 2.8 in favor of the structureless slow component.

**(B)  $C_2HD$ .** Figure 9 shows the raw spectra of the H-atom and D-atom channels from the dissociation of  $C_2HD$ . A quick glance over these spectra indicates that they are in accord with the general trend observed in Figure 6 for  $C_2H_2$  and  $C_2D_2$ . The central dip in the H-atom TOF spectra is deeper than that for the D-atom channel. Likewise, the H-atom spectrum also exhibits more pronounced structures. However, a closer inspection reveals that the structures observed for  $C_2HD + L\alpha \rightarrow C_2D + H$  are in fact the structures characteristic of the  $C_2H$

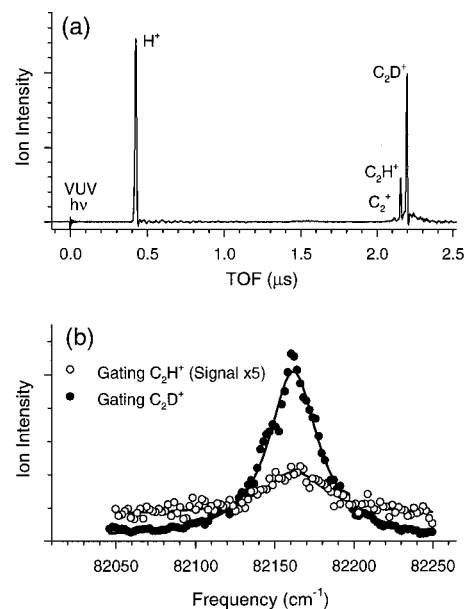
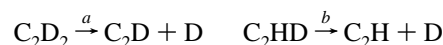


**Figure 10.** (a) Mass spectrum of  $C_2HD$  at 121.58 nm. (b) Photofragment action spectra of  $C_2D$  and  $C_2H$  for the photolysis of  $C_2HD$ . Solid lines are the Lorentzian fit, on top of a constant continuum background, of the spectra.

fragment, rather than  $C_2D$  cofragment. The isotopic purity of the  $C_2HD$  sample is better than 90% according to the manufacturer. Since the absorption cross section of  $C_2H_2$  at 121.6 nm could be substantially larger as alluded to earlier, a small amount of  $C_2H_2$  in the sample can make a significant contribution to the observed H-fragment yield.

Considering a  $C_2HD$  sample with small amounts of  $C_2H_2$ ,  $f$  relative to  $C_2HD$ , and  $f'$  amounts of  $C_2D_2$ , the photofragments H- and D-atoms can be generated from



The percentage of contamination due to  $C_2H_2$  impurities in detecting the H-atom is then  $(f\sigma^d/(\sigma^c + f\sigma^d))_{\lambda H}$ , where  $\sigma^i$  is the photodissociation cross section for the  $i$ th process in (14) and the subscript  $\lambda H$  indicates the cross sections at the H-atom L- $\alpha$  frequency. Thus, three quantities are needed to correct for its contribution to the observed spectra.

To achieve that, experiments were performed by operating the spectrometer in the mass mode, i.e., using high extraction voltage. Figure 10a shows the mass spectrum of the  $C_2HD$  sample at 121.58 nm, which was tuned away from the L- $\alpha$  transitions (both H and D atoms) in order to eliminate electronics ringing from the over-saturated  $H^+/D^+$  signal in the vicinity of neighboring mass peaks. Four fragment mass peaks can readily be identified. The  $H^+$  is from the (1 + 1) REMPI process near the Doppler wing. The observation of the other three peaks deserves some comments. The ionization potentials (IP) for  $C_2$  and  $C_2H$  are 12.1 and 11.5 eV, respectively,<sup>38</sup> which are higher than the VUV photon energy of 10.2 eV. Though one cannot completely rule out the possibility of multiphoton (e.g., UV + VUV) detection of these species, it is more likely that they come from the VUV photoionization of the internally excited fragments produced in the photodissociation of  $C_2HD$ . Note that the IP of  $C_2HD$  should be similar to that of  $C_2H_2$  (11.4 eV),<sup>38</sup> which is also larger than the 10.2-eV photon energy and no  $C_2HD^+$  was observed. With that caveat, integrating the mass peaks of  $C_2H^+$  and  $C_2D^+$  yields an estimate for the  $C_2D/$

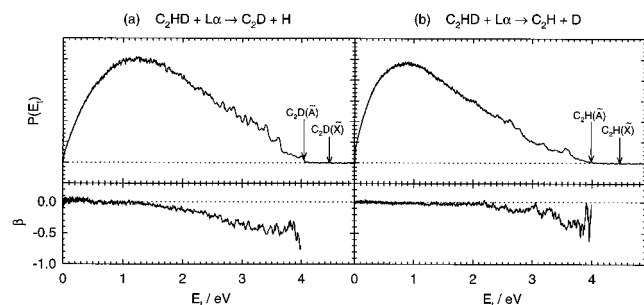


**Figure 11.** Photofragment c.m. translational energy distribution  $P(E_t)$  and the corresponding anisotropy distribution  $\beta(E_t)$  for the photolysis of C<sub>2</sub>HD when the (a) H- or (b) D-fragment was detected. The arrows mark the energetic thresholds for the corresponding electronic states of the fragment C<sub>2</sub>D/C<sub>2</sub>H.

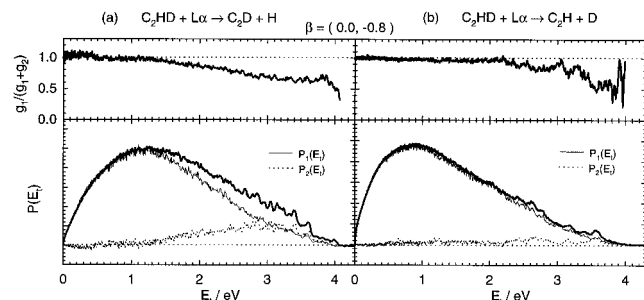


**Figure 12.** Partitioned  $P(E_t)$  for the photolysis of C<sub>2</sub>HD when either the (a) H- or (b) D-fragment was detected under the assumption of  $\beta_1 = 0$  and  $\beta_2 = -0.8$ . The upper panels show the resulting branching fraction, while the lower panels display the fragment translational energy distributions of the two corresponding pathways.

C<sub>2</sub>H ratio of 2.9 at that detuned wavelength ( $\lambda'$ ), which from (14) corresponds to  $(\sigma^c + f\sigma^a)_{\lambda'}/(\sigma^b + f\sigma^d)_{\lambda'} \approx \sigma_{\lambda'}^c/\sigma_{\lambda'}^b$ . Similar expressions can readily be obtained for the relative H(D)-atom yields for C<sub>2</sub>HD sample and for pure C<sub>2</sub>H<sub>2</sub> (C<sub>2</sub>D<sub>2</sub>) at  $\lambda_H$  ( $\lambda_D$ ).

To find out the photodissociation cross sections at various wavelengths the photofragment action spectra were taken, as shown in Figure 10b. Both spectra can be fitted with a Lorentzian function, on top of a constant continuum, centered at 82162 cm<sup>-1</sup> and with FWHM of 37 cm<sup>-1</sup>. This spectral feature is assigned to the C<sub>2</sub>HD,  $3R''2_0^1 \leftarrow X$  transition, which compares favorably to the results obtained recently by Welge and co-workers for C<sub>2</sub>H<sub>2</sub> (at 82 260 cm<sup>-1</sup> and 90 cm<sup>-1</sup> wide) and C<sub>2</sub>D<sub>2</sub> (at 82 100 cm<sup>-1</sup> and 24 cm<sup>-1</sup> wide) by detecting the H- or D-atom fragment in a two-color experiment.<sup>36</sup> Integrating the Lorentzian part of the spectral feature yields the ratio of C<sub>2</sub>D<sup>+</sup>/C<sub>2</sub>H<sup>+</sup> or H/D  $\approx 20$ , which is the “genuine” isotope ratio when C<sub>2</sub>HD is excited to the  $3R''2_0^1$  state. From the knowledge of the photodissociation cross sections at  $\lambda_H$ ,  $\lambda_D$ , and  $\lambda'$ , it can then be estimated that  $f \approx 0.03$ , a not unreasonable number, which yields about a 30% contribution of C<sub>2</sub>H<sub>2</sub> impurity to the H-atom detection of the C<sub>2</sub>HD sample! Such a large effect is due to the large disparity in the photodissociation cross section of two isotopic molecules at L- $\alpha$ .

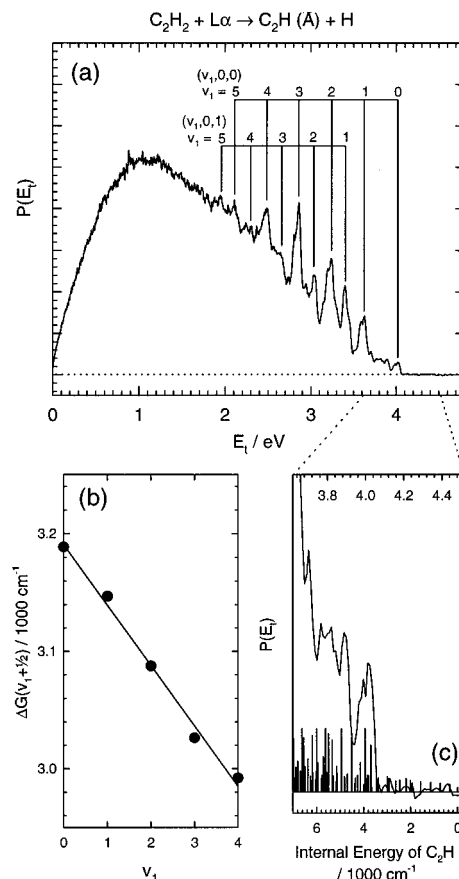
Figure 11 shows the  $P(E_t)$  and  $\beta(E_t)$  results for C<sub>2</sub>HD after the impurity corrections. The gross features lie in between the C<sub>2</sub>H<sub>2</sub> and C<sub>2</sub>D<sub>2</sub> results. Some minor structures remain in  $P(E_t)$  for the C<sub>2</sub>D + H channel. Due to the sharpness of the spectral features (Figures 6a and 9a) and the high sensitivity to the exact C<sub>2</sub>H<sub>2</sub> impurity contribution, it is not certain that they can all be assigned to the internal states of the cofragment C<sub>2</sub>D. A similar analysis was performed for the translational energy dependence of the  $\beta$  parameters. Figure 12 depicts the results.

Table 1 summarizes the atomic fragment yields and branching ratio of the fast and slow dissociation pathways for C<sub>2</sub>H<sub>2</sub> and

**TABLE 1: Summary of the Atomic Fragment Yields and the Corresponding Branching Ratios of the Fast and Slow Dissociation Pathways<sup>a</sup>**

	rel yields	slow H or D	fast H or D
C <sub>2</sub> H <sub>2</sub> + L- $\alpha$ $\rightarrow$ C <sub>2</sub> H + H	1	74%	26%
C <sub>2</sub> HD + L- $\alpha$ $\rightarrow$ C <sub>2</sub> D + H	0.102	63.5%	11%
C <sub>2</sub> HD + L- $\alpha$ $\rightarrow$ C <sub>2</sub> H + D	0.035	24%	1.5%
C <sub>2</sub> D <sub>2</sub> + L- $\alpha$ $\rightarrow$ C <sub>2</sub> D + D	0.039	100%	$\sim 0$

<sup>a</sup> The yield and branching ratio refer to the VUV laser at 82 259 cm<sup>-1</sup> (H-atom L- $\alpha$  transition) for the first two processes; similarly at 82 282 cm<sup>-1</sup> (D-atom L- $\alpha$  transition) for the last two processes.



**Figure 13.** (a) Assignments of the vibrational excitation of the C<sub>2</sub>H( $\tilde{A}$ ) state from the photolysis of C<sub>2</sub>H<sub>2</sub>. (b) Birge–Sponer plot of the assigned progression. (c) Expanded portion of  $P(E_t)$  in comparison with the theoretical results of Peric et al.<sup>48</sup> The height of the vertical sticks reflects the fraction of the II electronic state in the calculated vibronic wavefunctions.

the isotopic variants at L- $\alpha$  when either the H- or D-fragment is detected. Clearly, the relative yields reflect essentially the absorption characteristics which also govern the branching of the fast or slow dissociation pathway in a decisive manner.

**(C) Vibrational Assignment of C<sub>2</sub>H( $\tilde{A}$ ) and State Distribution.** The prominent structures observed in the product translational energy distribution ( $P(E_t)$ ) in the photolysis of C<sub>2</sub>H<sub>2</sub> reflect the internal state distribution of the C<sub>2</sub>H fragment. Readily assignable progressions of C<sub>2</sub>H( $\tilde{A}$ ) vibrational excitation are shown in Figure 13a. Owing to the resolution limit, the assignment of the bending excitations, i.e., the exact location for  $v_2 = 0$ , is somewhat ambiguous. Nevertheless, the Birge–Sponer analysis of the C–H stretching progression as shown in Figure 13b yields the spectroscopic constants of  $\omega_e$  and  $\omega_e x_e$  to be 3240 and 26 cm<sup>-1</sup>, respectively. And the spacing of about 1720 cm<sup>-1</sup> between the two progressions is taken to be the fundamental frequency of the C $\equiv$ C stretch of the electronically excited state C<sub>2</sub>H( $\tilde{A}$ ). To our best knowledge this is the first



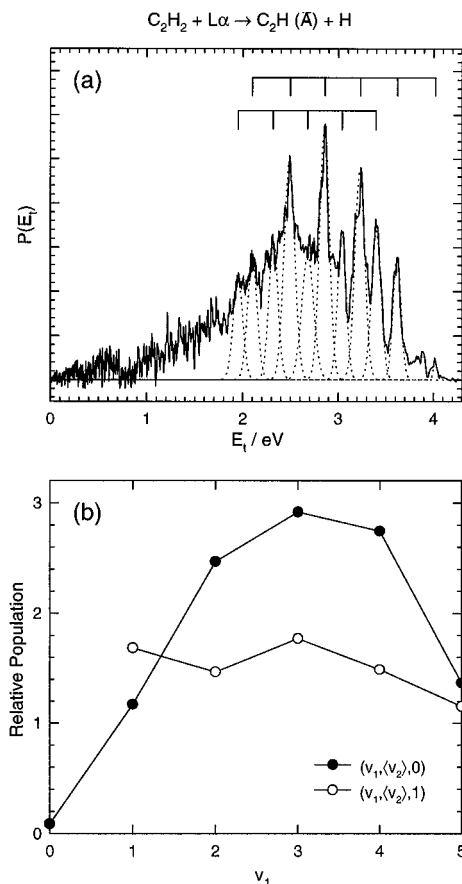


**Figure 14.** (a) Deconvoluted Gaussian peaks of the translational energy distribution of the fast dissociation pathway in the photolysis of  $C_2H_2$ . The caps denote the two assigned progressions. (b) Population analysis of the vibrational progressions of the  $C_2H(\tilde{A})$  fragment.

experimental determination of those vibrational frequencies for the  $\tilde{A}$ -state in the gas phase. The  $1720\text{ cm}^{-1}$  for the  $C\equiv C$  stretch compares favorably to that of  $1706\text{ cm}^{-1}$  obtained recently for  $C_2H(\tilde{A})$  in a neon matrix.<sup>39</sup>

Since the observed  $C_2H(\tilde{A})$  vibrational structures are attributed entirely to the fast dissociation pathway, a rough estimate of their distribution is shown in Figure 14a by deconvoluting the translational energy distribution of the fast dissociation pathway into separate Gaussian peaks. Not unexpectedly, the fit is not perfect. On the other hand, it is not totally unrealistic. The relative populations of two vibrational progressions thus obtained are plotted in Figure 14b. A clear mode-specific behavior is revealed. The excitation of the "pure" C–H stretching mode is inverted, peaking around  $v_1 \approx 3$ , whereas that for the combination bands of C–H and C $\equiv$ C stretches displays a rather flat distribution.

**(D) Photodissociation Dynamics.** There are two remarkable observations for the photodissociation of  $C_2H_2$  and isotopic variants at the L- $\alpha$  wavelength in this study. First, the dissociation of a photoexcited molecule appears to be governed by two distinct pathways characterized by different dissociation lifetimes and product energy distributions. In spite of the fact that at 121.6 nm different isotopic molecules exhibit very different photoabsorption features, which only determine the branching of these two dissociation pathways, they all show a strong propensity toward (against) the formation of the  $C_2H(\tilde{A})$  ( $C_2H(\tilde{X})$ ) fragment. This is in sharp contrast to the photodissociation of  $C_2H_2$  at 193 nm.<sup>40,41</sup> Second, while the slower pathway ( $\beta \approx 0$ ) yields a statistical-like product energy distribution, the faster one ( $\beta \approx -0.8$ ) produces a highly structural and mode-specific distribution.

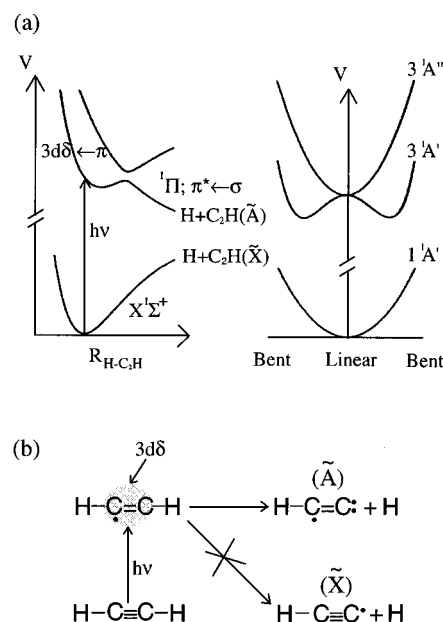


**Figure 15.** (a) Plausible PES's involved in the photolysis of  $C_2H_2$  at 121.6 nm, adapted from the HCN analogue by Morley *et al.*<sup>45</sup> See text for detail. (b) Schematic representation of the electronic configurations and rearrangements involved in the photodissociation process.

All previous spectroscopic investigations indicated that around 121.6 nm the absorption spectra of  $C_2H_2$  and isotopic variants are dominated by the  $3R''2_0^1 \leftarrow X$  vibronic transition superimposed on top of a weak continuum.<sup>8,9,36</sup> The nature of this weak continuum is unclear. To understand the fates and the dissociation dynamics of a photoexcited  $C_2H_2$ , one needs some knowledge about the potential energy surfaces (PES's) that are involved in the dissociation. The calculation of the PES's around the 10-eV region has not yet been done. However, such a calculation has been performed for HCN<sup>42–44</sup> which is isoelectronic to  $C_2H_2$ . Based on that calculation, Morley *et al.*<sup>45</sup> have elegantly elucidated the dissociation dynamics of HCN (DCN) at 121.6 nm in a beautiful experiment using the Rydberg H(D)-atom TOF detection scheme. There are, undoubtedly, many differences between HCN and  $C_2H_2$ . We do expect, however, the qualitative features of the PES's of HCN to apply in the case of  $C_2H_2$ . In particular, Morley *et al.*'s interpretation for the production of the CN(A) fragment seems to be valid here to rationalize the propensity toward the formation of  $C_2H(\tilde{A})$ . Part of their Figure 6 (ref 45) is reproduced here in Figure 15a for clarity. When the photoexcitation is in resonance, an excited  $3R''2_0^1$   $C_2H_2$  is formed. The Rydberg state  $3R''$  is of  $^1\Pi_u$  symmetry, arising from the  $3d\delta \leftarrow \pi$  orbital excitation; thus, it is subject to Renner–Teller (R–T) splitting into the  $^1A''$  and  $^1A'$  surfaces as the molecule bends. (For a tetraatomic molecule there are two doubly degenerate bending modes, the actual splitting is more complicated than shown here.)<sup>46</sup> Asymptotically, the ground state of ethynyl radical has a triple C $\equiv$ C bond with a  $\sigma$  unpaired electron, schematically depicted in Figure 15b, which correlates with the ground state of acetylene when a hydrogen atom approaches it. The excited  $C_2H(\tilde{A})$  state is of  $^2\Pi$  symmetry in linear geometry with a  $\pi$ -radical orbital and a lone pair electron of one of the carbon atoms. That state also is subject to R–T effects. For a collinear approach of the hydrogen atom the repulsive interactions between the lone-pair electrons and the H-atom electron result in a repulsive, valence-type PES, and avoided crossings with the Rydberg excited PES's occur at shorter C–H distances. This type of Rydberg–valence interaction is what Mulliken termed the "MO-or-state Rydbergization".<sup>15</sup> The avoided crossing is

the quantum mechanical representation of the rearrangement of the electronic configuration along the reaction coordinate. As cartooned in Figure 15b, the electronic configuration of an excited  $3R''$  Rydberg state can evolve rather smoothly into that of  $C_2H(\tilde{A}) + H$ , hence intuitively a facile process. The propensity toward the formation of  $C_2H(\tilde{A})$  is therefore interpreted as a manifestation of this strong electronic adiabaticity, just as the case for HCN dissociation.<sup>43</sup> The dominance of the  $\Pi$ -character surface in the dissociation dynamics also manifests itself near the post-threshold region for the formation of the  $C_2H(\tilde{A})$  state. It is known that the  $C_2H(\tilde{X})$  and  $C_2H(\tilde{A})$  states are perturbing each other in this region.<sup>47–49</sup> The eigenfunction is therefore a mixing of the two. Depicted in Figure 13c is the comparison between the experimental  $P(E_t)$  and theoretically calculated  $\Pi$ -character,<sup>48,49</sup> i.e., the fraction of the  $\Pi$  electronic state in the vibronic wavefunction, of the C<sub>2</sub>H radical around the threshold region. A constant shift of the  $\tilde{A}$ -state origin from the calculated value<sup>48</sup> of 3583 cm<sup>-1</sup> to the experimental value<sup>50</sup> of 3692 cm<sup>-1</sup> has been applied for the theoretical results. Clearly, the gross features of the observed  $P(E_t)$  are reproduced rather well from this electronic character consideration only.

It is perhaps more intriguing that the same propensity was also observed for C<sub>2</sub>D<sub>2</sub> and C<sub>2</sub>HD, for which the absorption of the L- $\alpha$  photon occurs in the continuum region. We speculate that the weak, continuum absorption arises from the unfavorable Franck–Condon transitions to the excited state in bent geometry; i.e., the excited state still possesses a large fraction of  $3R''$   $\Pi$ -state characters near the L- $\alpha$  region. Hence, the electronic adiabaticity is always invoked regardless of the initial excitation wavelengths or whether the dissociation proceeds via collinear (say A'') or bent (A') surfaces.

Clearly, those molecules dissociating on the A'' surface prefer a nearly collinear geometry. In accord with the observed large  $\beta$  value ( $-0.8$ ) the dissociation must be fast enough to compete with the bending motion. From the measured line width of the  $3R''2_0^1$  state for C<sub>2</sub>H<sub>2</sub> a dissociation lifetime of 58 fs is inferred by Welge and co-workers.<sup>36</sup> The effect of bending motion (on the excited state surface) on the fragment recoil anisotropy has also been investigated recently for a model triatomic system.<sup>51</sup> A rough estimate based on that simple model or using the  $\beta = 2P_2(\cos \alpha)$  approximation leads to 10°–15° deviation from linearity for the observed  $\beta = -0.8$  value. Thus, the fast dissociation pathway is pictured as a nearly collinear passage over the avoided crossing, followed by a steep repulsion between two dissociating fragments. Asymptotically, it yields an inverted distribution for the C–H stretching mode in accord with the Franck–Condon expectation of the C–H bond length change from the Rydberg-excited C<sub>2</sub>H<sub>2</sub> to the  $C_2H(\tilde{A})$  fragment. Since the initial excitation has one quantum of C $\equiv$ C vibration,<sup>9</sup> the prominent progression of the combination band with one quantum of C $\equiv$ C excitation suggests that some memory of the initial mode-excitation is retained in this fast dissociation pathway.

As to the slower pathway, dissociation may occur via the A' surface or the other low-lying Rydberg/valence surfaces following the radiationless processes. Either way it likely involves a long-lived intermediate in a bent geometry, resulting in a structureless and statistical-like product translational energy distribution due to the extensive intramolecular energy redistribution prior to dissociation, as well as an isotropic angular distribution. Yet, the “transition state” for this bent dissociation pathway could still originate from the avoided crossing with the repulsive, valence surfaces which correlate with  $C_2H(\tilde{A}) + H$  asymptotically. In all cases, the  $P(E_t)$  distributions for the

slow pathway peak around 1 eV, indicating the barrier height for that avoided crossing “transition state”.

#### IV. Conclusion

This paper described in details a newly-developed Doppler-selected TOF technique for measuring the product angular distribution from a photodissociative or a collisional process. The first application of this exceedingly simple technique for H-atom detection is demonstrated here and the result is very encouraging. Compared to the celebrated Rydberg H-atom TOF technique, our resolution is no better.<sup>26</sup> However, our goal is not to develop an alternative way for interrogating H-atom but is rather a more general scheme with comparable resolution for many other interesting species, which only requires one probe laser for REMPI detection. An on-going extension of this technique to the O-atom detection in this laboratory already revealed several intriguing, previously unobserved dynamical features in the study of the NO<sub>2</sub> photodissociation process.<sup>52</sup>

Using this technique it is found that the photodissociation of acetylene at L- $\alpha$  exhibits a strong propensity toward the formation of the  $C_2H(\tilde{A})$  fragment, similar to that for hydrogen cyanide. The involvement of a triatomic (rather than a diatomic) fragment here and the additional measurements of recoil anisotropy parameter and isotopic variants provide an opportunity to explore the dynamics further and to gain deeper insights. It appears that the dissociation mechanism originally proposed by Ashfold and co-workers for HCN,<sup>45</sup> i.e., the Rydberg–valence surface intersections, plays a decisive role in determining the dissociation dynamics of acetylene as well. Since acetylene exhibits rich, vibronically resolved spectroscopic features in the 110–150-nm region,<sup>8–10</sup> the planned two-color, tunable VUV experiment<sup>36</sup> will be very fruitful in elucidating further the role of Rydberg–valence interactions in a typical predissociation process.

**Acknowledgment.** The financial support from the U.S. Department of Energy and the National Science Council of Taiwan (NSC 86-2113-M-001-036) is gratefully acknowledged. We also thank Dr. Yen-Chu Hsu (IAMS) for the generous supply of the C<sub>2</sub>D<sub>2</sub> isotopic sample.

#### References and Notes

- Ingold, C. K.; King, G. W. *J. Chem. Soc. (London)* **1953**, 2702.
- Innes, K. K. *J. Chem. Phys.* **1954**, 22, 863.
- Fujii, M.; Haijima, A.; Ito, M. *Chem. Phys. Lett.* **1988**, 150, 380.
- Haijima, A.; Fujii, M.; Ito, M. *J. Chem. Phys.* **1990**, 92, 959.
- Mordaunt, D. H.; Ashfold, M. N. R. *J. Chem. Phys.* **1994**, 101, 2630.
- Hashimoto, N.; Suzuki, T. *J. Chem. Phys.* **1996**, 104, 6070.
- Foo, P. D.; Innes, K. K. *Chem. Phys. Lett.* **1973**, 22, 439.
- Suto, M.; Lee, L. C. *J. Chem. Phys.* **1984**, 80, 4824.
- Herman, M.; Colin, R. *Phys. Scr.* **1982**, 25, 275.
- Herman, M.; Colin, R. *J. Mol. Spectrosc.* **1981**, 85, 449.
- Sandorfy, C. *Topics Curr. Chem.* **1979**, 86, 91.
- Sandorfy, C. *J. Mol. Struct.* **1973**, 19, 183.
- Buenker, R. J.; Peyerimhoff, S. D. *Chem. Phys.* **1975**, 36, 415.
- Mulliker, R. S. *Chem. Phys. Lett.* **1977**, 46, 197.
- Mulliker, R. S. *Acc. Chem. Res.* **1976**, 9, 7.
- Yung, Y. L.; Allen, M.; Pinto, J. P. *Astrophys. J. Suppl. Sec.* **1984**, 55, 465.
- Okabe, H. *Can. J. Chem.* **1983**, 61, 850.
- Kern, R. D.; Xie, K. *Prog. Energy Combust. Sci.* **1991**, 17, 191.
- Peeters, J.; Look, H. V.; Ceusters, B. *J. Phys. Chem.* **1996**, 100, 15124.
- Pedersen, J. O. P.; Opansky, B. J.; Leone, S. R. *J. Phys. Chem.* **1993**, 97, 6822.
- Look, H. V.; Peeters, J. *J. Phys. Chem.* **1995**, 99, 16284.
- Koshi, M.; Fukuda, K.; Kamiya, K.; Matsui, H. *J. Phys. Chem.* **1992**, 96, 9839.
- Summers, M. E.; Strobel, D. F. *Astrophys. J.* **1989**, 346, 495.
- Opansky, B. J.; Leone, S. R. *J. Phys. Chem.* **1996**, 100, 4888.

- (25) Lai, L.-H.; Che, D.-C.; Liu, K. *J. Phys. Chem.* **1996**, *100*, 6376.  
(26) Zhang, J.; Riehn, C. W.; Dulligan, M.; Wittig, C. *J. Chem. Phys.* **1995**, *103*, 6815.  
(27) Lai, L.-H.; Wang, J.-H.; Che, D.-C.; Liu, K. *J. Chem. Phys.* **1996**, *105*, 3332.  
(28) Macdonald, R. G.; Liu, K. *J. Chem. Phys.* **1989**, *82*, 91.  
(29) Hilbig, R.; Wallenstein, R. *IEEE J. Quantum Electronics* **1981**, *QE-17*, 1506.  
(30) Wiley, W. C.; McLaren, I. H. *Rev. Sci. Instrum.* **1995**, *26*, 1150.  
(31) Thoman, Jr. J. W.; Chandler, D. W.; Parker, D. H.; Janssen, M. H. *M. Laser Chem.* **1988**, *9*, 27.  
(32) Houston, P. L. *Acc. Chem. Res.* **1989**, *22*, 309.  
(33) Mons, M.; Dimicoli, I. *J. Chem. Phys.* **1989**, *90*, 4037.  
(34) Yang, S.; Bersohn, R. *J. Chem. Phys.* **1974**, *61*, 4400.  
(35) Schinke, R. *Photodissociation Dynamics*; Cambridge University Press: New York, 1993.  
(36) Löffler, P.; Lacombe, D.; Ross, A.; Wrede, E.; Schnieda, L.; Welge, K. H. *Chem. Phys. Lett.* **1996**, *252*, 304.  
(37) Hwang, H. J.; El-Sayed, M. A. *J. Chem. Phys.* **1992**, *96*, 856.  
(38) Berkowitz, J. *Photoabsorption, Photoionization and Photoelectron Spectroscopy*; Accademic Press: New York, 1979.  
(39) Forney, D.; Jacox, M. E.; Thompson, W. E. *J. Mol. Spectrosc.* **1995**, *170*, 178.  
(40) Wodtke, A. M.; Lee, Y. T. *J. Phys. Chem.* **1985**, *89*, 4744.  
(41) Balko, B. A.; Zhang, J.; Lee, Y. T. *J. Chem. Phys.* **1991**, *94*, 7958.  
(42) Peric, M.; Buenker, R. J.; Peyerimhoff, S. D. *Mol. Phys.* **1988**, *64*, 843.  
(43) Vazquez, G. J.; Gouyet, J. F. *Chem. Phys. Lett.* **1978**, *57*, 385.  
(44) Vazquez, G. J.; Gouyet, J. F. *Chem. Phys. Lett.* **1979**, *65*, 515.  
(45) Morley, G. P.; Lambert, I. R.; Ashfold, M. N. R.; Rossev, K. N.; Western, C. M. *J. Chem. Phys.* **1992**, *97*, 3157.  
(46) Colin, R.; Herman, M.; Kopp, I. *Mol. Phys.* **1979**, *37*, 1397.  
(47) Stephens, J. W.; Yan, W.-B.; Richnow, M. L.; Solka, H.; Curl, R. F. *J. Mol. Struct.* **1988**, *190*, 41.  
(48) Peric, M.; Peyerimhoff, S. D.; Buenker, R. J. *J. Mol. Spectrosc.* **1991**, *148*, 180.  
(49) Peric, M.; Peyerimhoff, S. D.; Buenker, R. J. *Z. Phys. D* **1992**, *24*, 177.  
(50) Pfelzer, C.; Havenith, M.; Peric, M.; Murtz, P.; Urban, W. *J. Mol. Struct.* **1988**, *190*, 41.  
(51) Loock, H.-P.; Cao, J.; Qian, C. X. W. *Chem. Phys. Lett.* **1993**, *206*, 422.  
(52) Hsich, C. H.; Lee, Y. S.; Fujii, A.; Lee, S. H.; Liu, K., unpublished work.